Xie Zhiqing (Orcid ID: 0000-0001-5294-4693)

Spatial Scales of Heavy Meiyu Precipitation Events in Eastern China and Associated Atmospheric Processes

Y. Du[1], Z. Q. Xie[2]*†, and Q. Miao[2]

[1] Key Laboratory of Meteorological Disaster, Ministry of Education, International Joint Laboratory on Climate and Environment Change, Collaborative Innovation Center on Forecast and Evaluation of Meteorological Disasters, Climate Dynamics Research Center, Nanjing University of Information Science and Technology, Nanjing 210044, China.

[2] Jiangsu Climate Center, Nanjing, 210009, China.

Corresponding author: Z. Q. Xie (xiezhiqing9896@163.com)

Key Points:

- Flood-related heavy Meiyu precipitation events have robust climatological spatial scales over eastern China
- An upper westerly jet stream and lower Meiyu front steer the position and orientation of rain-belts of heavy Meiyu precipitation events
- Convective activities along the Meiyu front zone have a comparable spatial scale to the rain-belt of heavy Meiyu precipitation events

Abstract

Analysis of ground-based and remotely retrieved precipitation data reveals that heavy Meiyu precipitation events (HMPEs) produce a relatively independent rain-belt over eastern China. A rotating calipers algorithm is applied to quantify the spatial scales of HMPEs. We find that HMPEs have regular spatial scales with an average length, width and extent of about 1400 km, 500 km and 40.00×10^4 km^2, respectively, through a comprehensive assessment of different types of HMPE, illustrating that HMPEs have a size similar to that of the sub-synoptic-scale Meiyu front (1500–2000 km). Convective activities along the Meiyu front zone and the upper westerly jet stream strongly affect the position and orientation of rain-belts of HMPEs. The Meiyu front zone, strong vertical motions and large transport of warm moisture have a comparable spatial scale to the HMPE rain-belts over eastern China.

Plain Language Summary

Many studies have revealed that extreme precipitation events of short or long duration have highly varying spatial scales from several hundred kilometers to several thousand kilometers, increasing the difficult of identifying the most flood-related precipitation events and corresponding important atmospheric processes. We used a rotating calipers algorithm to quantify the length, width, position and orientation of rain-belts and found that flood-related heavy Meiyu precipitation events with strong intensity, long duration and large area have regular climatological spatial scales. Our results will benefit flood-risk management and decision making for the Yangtze River Basin in China.

1 Introduction

Understanding the spatial scale of extreme precipitation events (EPEs) is important in mitigating flood risks. The spatial scale of EPEs affects the size of the potential flooding region and is thus important to a basin's hydrologic response and flooding-risk management (Konrad and Charles, 2001; Houze et al., 2015). Theoretically, different EPEs should match atmospheric processes on a rational spatial scale (Olanski, 1975). As examples, a persistent Meiyu (also known as Baiu) precipitation event in 2016 was associated with the Meiyu front situating stably in the Yangtze River Basin and triggered a record-breaking severe flood disaster (Li et al., 2018); a severe flooding event in Washington and Oregon in December 2007 was associated with a sequence of storm events hitting the same area over 3 days (Neiman et al., 2008, 2011); and a 2010 intense precipitation event over Pakistan resulted from a sequence of monsoon surges and southward intruding extra-tropical circulation anomalies (Hong et al., 2011).

When EPEs are identified by their lifetime and/or intensity, they include many small-size or short-lifetime precipitation events and thus vary strongly on spatial scales. Climatological length scales of extreme daily precipitation events were shown to be in the range of 200–400 km over the eastern United States (Touma et al., 2018). Two-day heavy precipitation events that were most closely related to flood damage over the United States had a highly varying spatial extent of 0.25×10^4–50.0×10^4 km^2 (Pielke and Downton, 2000; Konrad and Charles, 2001). Across the globe, short precipitation events lasting less than 1 day had spatial extents ranging from 0.31×10^4 to 3.8×10^4 km^2 while long precipitation events lasting about 1–5 days had spatial extents of 0.31×10^4–15.0×10^4 km^2 according to global Tropical Rainfall Measuring Mission satellite data (White et al., 2017). These strongly varying spatial scales are notably associated with different atmospheric processes from mesoscale to synoptic scale.

We cannot identify the EPEs most related to floods and the corresponding important atmospheric processes, which is detrimental to flood-risk management.

Over eastern China, flood-related heavy Meiyu precipitation events (HMPEs) generally last about 3–7 days and extend zonally from several hundred kilometers to several thousand kilometers across eastern China to southern Japan (Chen et al., 2016; Yang et al., 2016). They have a low frequency of occurrence but tend to trigger severe flood disasters over the Yangtze–Huaihe Basin owing to their long duration, large area and high rainfall (Xie et al., 2018). For many years, the mechanisms of HMPEs have been topics of research on the East Asian summer monsoon. Previous studies have highlighted that more knowledge of the synoptic-scale systems contributing to persistent precipitation extremes is required to predict HMPE-related flood risk over eastern China (Zhou et al. 2009; Chen and Zhai 2016). HMPEs are generally accompanied by an extended eastward South Asia High at the 100-hPa level, strong westerly jet at the 200-hPa level, western Pacific subtropical high (WPSH) at the 500-hPa level, and large northeastward moisture fluxes in the lower atmosphere (Sampe and Xie, 2010). Seasonal zonal extensions and retractions of the WPSH western flank, driven by atmospheric teleconnections and local air–sea interaction (Guan et al., 2019), particularly affect the position and orientation of Meiyu rain-belts over eastern China. Compared with the physical mechanisms of HMPEs, much less attention has been paid to the spatial scale of HMPEs.

Comprehensive spatial features of the HMPE rain-belt, including the length, width, extent, position and orientation, would be helpful in predicting the potential flooding regions and are important in understanding the physical mechanism of HMPEs and correspondingly atmospheric processes. As the primary HMPE-producing weather system, the Meiyu front strongly affects the size and orientation of HMPE rain-belts and has been extensively investigated in large-, synoptic- and meso-scale studies (Li et al., 2018). The Meiyu front is

characterized by a weak temperature gradient and a strong wind shear over eastern China whereas it is characterized by a strong temperature gradient near Japan (Ding, 1992). Correspondingly, most rain falls south of the Meiyu front in eastern China and north of the Meiyu front in southern Japan (Li et al., 2018**)**. HMPEs may therefore have their own unique spatial features over eastern China from synoptic and dynamics viewpoints, but this has not yet been well verified by climatological observation studies. Organized mesoscale convective storms propagating along the stationary Meiyu frontal zone in a few days are mainly response for persistent EPEs (Ding and Chan, 2005). They generate a small rain-belt of approximately 100–600 km over eastern China on an hourly scale (Li, 2016) and form a long rain-belt of several hundred or thousand kilometers in a few days (Chen et al., 2016; Yang et al., 2016). Many HMPEs triggering flood damage over the Yangtze–Huaihe Basin have had a spatial length close to that of the Meiyu front (1500–2000 km) (Ding et al., 2007; Nimoniya and Shibagaki, 2007). It is confusing which length scale is most representative of HMPEs over eastern China and what atmospheric processes determine the spatial scale of HMPEs. In this study, we primarily (1) quantify the spatial scales of HMPEs using the rotating calipers algorithm developed by Toussaint (1983) based on a 0.25° × 0.25° gridded long-term precipitation dataset for 1955–2015 released by the China Meteorology Administration (CMA, Shen and Xiong, 2015) and (2) investigate spatial features of the dominant HMPE types and associated atmospheric thermodynamic processes.

2 Materials and Methods

2.1 Identifying HMPEs from the combination of the rainfall intensity, duration and area

Previous studies defined flood-related HMPEs as events lasting longer than 3 days and having areas in which precipitation is at least 50 mm exceeding 10^5 km^2 over the Meiyu region of [28°N –34°N, 110°E–123°E] (Wang and Hu, 1993; Chen et al., 2017; Zhou et al.,

2017). This criterion was applied to identify HMPEs in the present study. A 3-day moving-window algorithm was firstly applied to find all 3-day precipitation events with the rainfall area of at least 50 mm exceeding 10^5 km^2 in the Meiyu seasons of 1955–2015. HMPE datasets were then obtained after merging those 3-day heavy precipitation events with date overlap into corresponding continuous-precipitation events.

2.2 Characterizing the spatial scales of rain-belts applying the rotating calipers algorithm

The rotating calipers algorithm (Toussaint, 1983) and contour tracing algorithm (Wang, 2012) were applied to find the minimum-area enclosing rectangle of each core with precipitation exceeding 50 or 100 mm for all HMPEs in 1955–2015. These rectangles were then used to quantify the extent, length, width and orientation of the HMPE rain-belt.

First, the contour tracing algorithm was applied to find all precipitation centers having a total rainfall amount exceeding 50 and 100 mm for each HMPE and their corresponding convex polygons were extracted. A cubic spline-smoothing algorithm was applied subsequently to eliminate narrow sharp corners of each convex polygon.

The rotating calipers algorithm was then applied to find the minimum-area enclosing rectangle of each convex polygon and its minimum rotating angle from the horizontal axis.

Finally, the long and short sides, rotating angle and rainfall area of the minimum-area enclosing rectangle were used to represent the length, width, orientation and extent of the rain-belt of an HMPE. An example is shown in Figure 1a for the HMPE that occurred on 15–17 June 1996. Spatial features of the rain-belt of an EPE, in terms of length, width, extent, position and orientation, are important in estimating the flood risk and potential flooding region. Compared with methods based on the indicator semivariogram (Touma et al., 2018) and square root of the rainfall area (Li et al., 2016), which focus simply on the length scale of

an EPE rain-belt, the rotating calipers algorithm more comprehensively obtains spatial features of the rain-belt, including the length, width, extent, position and orientation.

3 Data

Long-term gridded precipitation datasets with a fine spatial scale are especially useful in inferring the spatial scales of EPEs because they provide a uniform spatial coverage (Ensor and Robeson, 2008). A 0.25° × 0.25° ground-based gridded precipitation dataset for 1955–2015 (Shen and Xiong, 2015) was used to examine the spatial scales of the HMPEs. Datasets of precipitation estimated from remotely sensed information using artificial neural networks (PERSIANN; Ashouri et al., 2015) and the Climate Prediction Center morphing method (CMORPH; Joyce et al., 2004) and taken from the Tropical Rainfall Measuring Mission (TRMM 3B42; Huffman et al., 2007) were used to validate whether the HMPEs create an independent rain-belt over eastern China. Daily outgoing longwave radiation (OLR) data (Schreck et al., 2018) were used to validate convective activities related to the HMPEs. Meteorological parameters of the wind speed, temperature, height and specific humidity with a resolution of 0.75° × 0.75° were obtained from the ERA-Interim project of the European Centre for Medium Range Weather Forecasts (Dee et al., 2011) and adopted as primary data for diagnosing the mechanism of HMPEs.

4 Results

4.1. Climatology of spatial scales of the HMPEs

Applying the methods described in section 2, we obtained 375 HMPEs for the period 1955–2015, among which there were 489 and 310 samples for 50- and 100-mm rain-belts respectively. The durations of these HMPEs ranged from 3 to 8 days and averaged 4 days. The length, width and extent of 50-mm rain-belts respectively ranged 312.5–2583.2 km, 206.6–1424.5 km and 6.6×10^4–108.1×10^4 km^2 and respectively averaged 1373.0 km, 541.1 km and 40.0×10^4 km^2 (Table 1). Those sample distributions showed a clear peak at 1391.0

km, 481.0 km and 39.0 × 10^4 km^2 respectively (Figure 1b), meaning that HMPEs have unique spatial scales over eastern China. The 50-mm rain-belts of HMPEs had a large occurrence of about more than 200 over the Yangtze River Basin (Figure 1c), with the average orientation of about 14.8° being close to the orientation of the Yangtze River of about 14.97° (Table 1). The 100-mm rain-belts of HMPEs had a spatial distribution similar to that of the 50-mm rain-belts, with the average length, width and extent of about 823.5 km, 285.3 km and 13.4 × 10^4 km^2 respectively (figure omitted). HMPEs were therefore prone to trigger flooding disasters in the Yangtze River Basin. Comparing with the spatial size of the 100-mm rain-belt, the 50-mm rain-belt of HMPEs had a length scale closer to the sub-synoptic-scale Meiyu front size (1500–2000 km). The length, width and spatial extent of about 1400 km, 500 km and 40.00 × 10^4 km^2 of 50-mm rain-belts therefore represent the climatological spatial scales of the HMPEs.

Figure 1d shows that the rain-belt of HMPEs varied strongly in terms of the orientation and length scale, because HMPEs mainly result from organized meso-α-scale (200–2000 km) convective storms along the Meiyu front (Ding and Chan, 2005; Li, 2016). The rain-belt of HMPEs mainly had a zonal pattern and tilted pattern with a southwest–northeast or northwest–southeast orientation owing to the anchoring systems of the 200-hPa westerly jet stream and the 500-hPa WPSH, and occasionally also had a meridional pattern because of the interaction between the Meiyu frontal systems and tropical cyclones (Xie et al., 2018). Sample distributions of the orientation of 50-mm rain-belts showed two breaks at about 12° and 34° (Figure 1b). We classify the HMPEs based on their rain-belt orientations by applying the Jenks–Fisher natural-break algorithm, which detects the best breaks by maximizing similarity within a class and differences between classes (Jenks, 1977). Two breaks were detected at 13.2° and 35.0°. These breaks divided all HMPEs into a zonal pattern [0.0°–13.2°), tilted pattern [13.2°–35.0°) and meridional pattern [35.0°–90.0°] (Figure 1d). The

zonal and tilted patterns accounted for 52.15% and 40.08% of the HMPEs and had a similar spatial scale (Table 1 and Figure 1d).

4.2. Validation of HMPE spatial scales from satellite-retrieved precipitation

The CMA ground-based precipitation dataset was available for mainland China. Compared with ground-based precipitation data, satellite-retrieved precipitation data provide more complete coverage from continents to oceans and capture similar spatiotemporal patterns of precipitation extremes in eastern China (Miao et al., 2015). We validated HMPE spatial scales by assessing whether the HMPEs form a relatively independent rain-belt over eastern China using PERSIANN, CMORPH and TRMM precipitation data. The satellite-retrieved precipitation data cannot be directly used to quantify the HMPE spatial scales because of their considerable uncertainty in rainfall intensity (Timmermans et al., 2019).

Three centers of average precipitation of at least 50 mm were located in northeastern India, the Yangtze River Basin, and southern Japan and the East China Sea respectively for the HMPEs according to PERSIANN, CMORPH and TRMM precipitation data (Figure 2a–2f). The precipitation center over eastern China was independent of that over southern Japan and the two were approximately divided by the eastern coastline of Asia. We further assessed the spatial distribution of precipitation for each HMPE; about 85.19% of HMPEs had an independent precipitation center over eastern China in the PERSIANN data of 1983–2015 while about 95.16% did so in the CMORPH and TRMM 3B42 data of 1998–2015. Furthermore, the spatial distribution of the OLR values provided evidence for HMPEs having their own spatial scales over eastern China (Figure 2g–2h). Regions of intense convection were located over eastern China in zonal and tilted HMPEs, where the OLR values were below 180 W m^{-2} and the proportion of OLR values below 240 W m^{-2} exceeded 80%, corresponding well to the domination of convective precipitation in the Meiyu rainfalls (He and Liu, 2016).

4.3. Effect of atmospheric structures on the HMPE spatial scale

The meridional pattern had low occurrence that was less than 10% of all HMPEs, and its spatial scale was associated with the tropical cyclones/typhoons landing over eastern China in the Meiyu season. Zonal and tilted patterns were dominant among the HMPEs and their rain-belts had similar spatial sizes over eastern China (Table 1). Identifying the key synoptic-scale conditions of zonal and tilted HMPEs is potentially fruitful in terms of clarifying the spatial scales of HMPEs. The weather systems related to HMPEs comprise an extended eastward South Asia High at the 100-hPa level, strong westerly jet at the 200-hPa level, WPSH at the 500-hPa level and large moisture fluxes in the lower atmosphere (Sampe and Xie, 2010). They had notably different configurations in zonal and tilted HMPEs over East Asia and the western North Pacific (Figure 3), which strongly affected the size and orientation of HMPE rain-belts according to a composite analysis of ERA-Interim data for 1983–2015.

In the upper atmosphere at 200-hPa level, the westerly jet stream of zonal HMPEs had a zonal pattern from western China to western North Pacific, with the strongest center being over eastern China (Figure 3a). Weak meridional winds with speeds of about 6 m s^{-1} slightly affected the shape and orientation of the jet stream at 30°N–45°N. Correspondingly, a zonal rain-belt appeared at the south of the jet stream. A large area of eastern China between 20°N and 40°N received more than 40 mm of rain, with the maximum rainfall exceeding 60 mm. For the tilted HMPEs (Figure 3b), the relatively weak jet stream had a V-shape structure over East Asia and the western North Pacific at 30°N–45°N, with strong meridional winds of the speed exceeding 9 m s^{-1} along the jet stream. Consequently, a tilted 40-mm rain-belt appeared south of the 200-hPa westerly jet stream, covering regions from western China to southern Japan. In the middle and lower atmosphere, the 500-hPa WPSH northern rim extended flatly from southwestern China to southern Japan, which was important in sustaining the west–east-orientated Meiyu front zone and strong moisture fluxes for zonal

HMPEs (Figure 3c). The strong vapor transport at the 850-hPa level from the Bay of Bengal and western Pacific merged at the Yangtze River Basin, accompanied by a strong zonal convective zone with ω exceeding −0.12 Pa s^{-1} at the 500-hPa level. Tilted HMPEs were associated with a northeastward flank of the WPSH from southwestern China to southern Japan (Figure 3d). A strong southwesterly along the WPSH northwestern flank transported large moisture vapors to eastern China and showed a similar orientation to the Meiyu front and convective zone (Figure 3d), and thus formed a tilted rain-belt.

Figure 3a–3d shows two characteristics shared by the zonal and tilted HMPEs. Firstly, the rain-belt, 500-hPa vertical velocities and 850-hPa Meiyu front zone had similar orientations over eastern China and the western North Pacific, which are associated with the dynamic effect of the WPSH northwestern flank and the 200-hPa westerly jet stream. Secondly, the Meiyu front zone, strong vertical motions and large transport of warm moisture had a spatial scale comparable to that of the HMPE rain-belts in terms of length, width and area. Similar spatial distributions of the 500-hPa vertical velocity and 850-hPa Meiyu front zone were seen in the northern part of the vapor transport over eastern China, with the vertical velocity exceeding −0.12 Pa s^{-1} and the equivalent potential temperature meridional gradient $\left|\frac{\partial \theta_e}{\partial y}\right|$ exceeding 3.0 °C per 100 km (Figure 3c–3d). A strong 850-hPa southwesterly flow transported a large amount of moisture to eastern China and created a thick moisture layer up to the 500-hPa level at 25°N–35°N (Figure 3g–3h). The strong upward motions and vapor transport at 850–300-hPa levels were capped by a strong divergence south of the upper jet stream at 25°N–35°N (Figure 3g–3h). There was a narrow convergence zone inclining northward between uplifting and sinking areas at 850–200-hPa levels, with strong wind shears and cold air intrusions at the lower right of the upper jet stream. Strong convective activities were located between the upper-level divergence and the mid- and lower-level convergences. Correspondingly, the maximum rainfall appeared along the strong vapor fluxes

at south of the upper jet stream. More importantly, the width of the area of the crossing of strong vertical velocities and large vapor fluxes at 850–300-hPa levels was approximately 500–600 km, which was close to the climatological width of HMPE rain-belts.

Defining the atmospheric pattern of zonal HMPEs as the basic state, notable differences in circulation between the zonal and tilted HMPEs were well depicted by the anomalies in total atmosphere sensible heating and the Rossby wave activity flux proposed by Takaya and Nakamura (2001). The distribution of 500-hPa height anomalies showed two Rossby wave trains at mid-latitudes and high latitudes between 30°E and 170°E (Figure 3e). The mid-latitude wave train clearly appeared along the jet stream at 30°N–60°N. Anomalies of total-atmosphere sensible heating had a spatial distribution similar to that of 500-hPa wave trains. In particular, the 200-hPa meridional wind showed a more remarkable wave train than the anomalies of 500-hPa height and total atmosphere sensible heating along the jet stream at mid-latitude, and this wind modulated the jet stream shape and orientation (Figure 3f). To examine a possible upstream effect on the formation of tilted HMPEs, we plot the distribution of the 200-hPa Rossby wave activity flux, which delineated the propagation eastward of wave activity along the jet stream from the Middle East to the western North Pacific (Figure 3f). Corresponding to the strong height and velocity anomalies in tilted HMPEs, the strongest wave activity appeared over western China and the western North Pacific. Two open ridges appeared over the Tibet Plateau–Mongolia region and Japan Sea, coupling with a deep trough from northeastern China to the Yangtze River, which corresponded well to the atmosphere-blocking structure of Meiyu–Baiu systems proposed by Nimomiya and Shibagaki (2007).

5 Conclusions

Precipitation becomes more spatially continuous over longer time periods and larger areas, making temporal accumulation more amenable to spatial-scale analysis and the identification of important atmospheric processes easier. The present paper defined HMPEs

as precipitation events lasting longer than 3 days with the 50-mm precipitation area exceeding 10^5 km^2 over the Meiyu region of China. This criterion combines the characteristics of a long duration, strong intensity and large area in identifying HMPEs and is more favorable for quantifying the spatial features of rain-belts in terms of the length, width, extent, position and orientation. The present study found that HMPEs had a spatial length, width and extent of about 1400 km, 500 km and 40.0×10^4 km^2, respectively, among which the length scale was close to the sub-synoptic-scale Meiyu front size of about 1500–2000 km. A validation analysis of precipitation spatial patterns using PERSIANN, CMORPH and TRMM precipitation data revealed that HMPEs generated a relatively independent rain-belt over eastern China, illustrating that the HMPEs have their own spatial scales over eastern China.

The location, shape and orientation of the 200-hPa westerly jet stream and the dynamic effect of the WPSH northwestern flank steer the orientations of vertical motions, Meiyu front and rain-belt of HMPEs. The Meiyu front zone, strong vertical motions and large transport of warm moisture had a spatial scale comparable to that of the 50-mm rain-belt of HMPEs over eastern China in terms of the length, width and area. The Tibet Plateau and western North Pacific at mid-latitudes are important regions in depicting the difference in atmospheric structure between zonal and tilted HMPEs. Total-atmosphere sensible heating and Rossby wave activity flux produced a mid-latitude wave train along the jet stream between 30°E and 170°E in tilted HMPEs because strong positive/negative tropospheric heating generally induces high/low pressure in the upper troposphere and the propagation eastward of wave activity along the jet stream amplified the blocking ridges in the areas of converging wave-activity flux. Consequently, fluctuations at the 500-hPa level produced two atmospheric blocking ridges over the Tibet Plateau–Mongolia region and Japan Sea and dynamically steered the orientation of the Meiyu front, strong convective zone and the rain-belts of tilted HMPEs.

Previous research showed that EPEs of the same or different duration have a varying spatial extent and length. However, flood-related HMPEs over eastern China, generally lasting more than 3 days with the 50-mm precipitation area exceeding 10^5 km^2, had robust climatological spatial scales that match corresponding weather systems of the Meiyu front. The rotating calipers algorithm extracts the length, extent, width and orientation of a rain-belt and thus provides comprehensive spatial features of the EPEs for identifying the potential flooding region and corresponding important atmospheric processes. Future research should quantify the climatological spatial scales of flood-related EPEs over high-flood-risk regions across the globe and thus improve the management of flood risk.

Acknowledgments

This work was supported by the National Natural Science Foundation of China (Grant 41930969 and 41205063), National Basic Research Program of China (973 Program) (Grant 2015CB453200), and Key Project of Jiangsu Meteorological Bureau (Grant KZ201903). The data used in this study are freely available from the China Meteorology Administration (http://data.cma.cn/en), NOAA atmospheric climate data record program (https://www.ncdc.noaa.gov/cdr/atmospheric/precipitation-persiann-cdr; https://www.ncdc.noaa.gov/cdr/atmospheric/precipitation-cmorph), Tropical Rainfall Measuring Mission (https://gpm.nasa.gov/TRMM), outgoing longwave radiation climate data record (http://olr.umd.edu), and the ECMWF website (https://www.ecmwf.int/en/forecasts/datasets/reanalysis-datasets/era-interim) .

References

Ashouri, H., K. Hsu, S. Sorooshian, D. K. Braithwaite, K. R. Knapp, L. D. Cecil, B. R. Nelson, and O. P. Prat (2015), PERSIANN-CDR: Daily precipitation climate data record from multisatellite observations for hydrological and climate studies, *Bull. Amer. Meteor. Soc.*, 96, 69–83, doi:10.1175/BAMS-D-13-00068.1.

Chen, X. Y., X. K. Zou, and Q. Zhang (2017), Grades of rainstorm disaster (in Chinese), *National Standard of the People's of China*, GB/T33680–2017.

Chen, Y., and P. M. Zhai (2016), Mechanisms for concurrent low-latitude circulation anomalies responsible for persistent extreme precipitation in the Yangtze River Valley. *Clim Dyn,* 47:989–1006.

Dee, D. P., with 35 co-authors (2011), The ERA-Interim reanalysis: configuration and performance of the data assimilation system, *Quart. J. R. Meteorol. Soc.*, 137, 553–597.

Ding, Y. H. (1992), Summer monsoon rainfalls in China, *J. Meteor. Soc. Japan.*, 70, 373–396.

Ding, Y. H., and C. L. Chan (2005), The East Asian summer monsoon: an overview, *Meteorol. Atmos. Phys.*, 89, 117–142.

Ding, Y. H., J. J. Liu, Y. Sun, Y. J. Liu, J. H. He, and Y. F. Song (2007). A study of the synoptic-climatology of the Meiyu system in East Asia, *Chin. J. Atmos Sci.,* 31(6), 1082–1101. (in Chinese)

Ensor, L. A., and S. M. Robeson (2008), Statistical characteristics of daily precipitation: Comparisons of gridded and point datasets, *J. Appl. Meteorol. Clim,* 47 (9), 2468–2476.

Guan, W. N, H. B. Hu, X. J. Ren, and X. Q. Yang (2019), Subseasonal zonal variability of the western Pacific subtropical high in summer: climate impacts and underlying mechanisms. *Clim Dyn*, 53, 3325–3344, doi:10.1007/s00382-019-04705-4.

He, J. H., and B. Q. Liu (2016), The East Asian subtropical summer monsoon: recent progress, *J. Meteor. Res.*, 30(2), 135–155, doi: 10.1007/s13351-016-5222-z.

Hong, C. C., H. H. Hsu, N. H. Lin, and H. Chiu (2011), Roles of European blocking and tropical-extratropical interaction in the 2010 Pakistan flooding, *Geophy. Res. Lett.*, L13806, doi: 10.1029/2011GL047583.

Houze, R. A., K. L. Rasmussen, M. D. Zuluaga, and S. R. Brodzik (2015), The variable nature of convection in the tropics and subtropics: A legacy of 16 years of the Tropical Rainfall Measuring Mission satellite, *Rev. Geophys., 53,* 994–1021, doi:10.1002/2015RG000488.

Huffman, G. J., D. T Bolvin, E. J. Nelkin, D. B. Wolff, R. F. Adler, G. Gu, Y. Hong, K. P. Bowman, and E. F. Stocker (2007), The TRMM multisatellite precipitation analysis (TMPA): Quasi-global, multiyear, combined-sensor precipitation estimates at fine scales,

J. Hydrometeorol., 8, 38–55.

Jenks, G. F. (1977), Optimal data classification for choropleth maps. *Department of Geography Occasional Paper no. 2*. Lawrence: University of Kansas.

Joyce, R. J., J. E. Janowiak, P. A. Arkin, and P. P. Xie (2004), CMORPH: A method that produces global precipitation estimates from passive microwave and infrared data at high spatial and temporal resolution, *J. Hydrometeor.*, 5(3), 487–503.

Konrad II, and E. Charles (2001), The most extreme precipitation events over the Eastern United States from 1950 to 1996: considerations of scale, *J. Hydrometeorol.*, (2), 309–325.

Li, N. N. (2016), Analyses of the precipitation spatial scale features over the contiguous China, *Master thesis: Chinese Academy of Meteorological Sciences*, Beijing.

Li, Y. N., Y. Deng, S. Yang, and H. N. Zhang (2018), Multi-scale temporal-spatial variability of the East Asian Meiyu-Baiu fronts: characterization with a suite of new objective indices, *Clim. Dyn.*, 51(5–6), 1659–1670, doi:10.1007/s00382-017-3975-4.

Miao, C. Y., H. Ashour, K. L. Hsu, H. Sorooshian, and Q. Y. Duan (2015), Evaluation of the PERSIANN-CDR Daily rainfall estimates in capturing the behavior of extreme precipitation events over China, *J. Hydrometerol.*, 16(3), 1387–1396.

Neiman, P. J., F. M. Ralph, G. A. Wick, Y. H. Kuo, T. K. Wee, Z. Z. Ma, G. H. Taylor, and M. D. Dettinger (2008), Diagnosis of an intense atmospheric river impacting the Pacific Northwest: Storm summary and offshore vertical structure observed with COSMIC satellite retrievals, *Mon. Weather. Rev.*, 136, 4398–4420.

Neiman, P. J., L. J. Schick, F. M. Ralph, M. Hughes, and G. A. Wick (2011), Flooding in Western Washington: the connection to atmospheric rivers, *J. Hydrometeorol.*, 12, 1337–1358.

Nimomiya, K., and Y. Shibagaki (2007), Multi-scale features of the Meiyu-Baiu front and associated precipitation systems, *J. Meteor. Soc. Japa*n, 85B, 103–122.

Orlanski, I. (1975), A rational subdivision of scales for atmospheric processes, *Bull. Amer. Meteor. Soc.*, 56(5), 527–530.

Pielke, J. R., and M. W. Downton (2000), Precipitaton and damaging floods: Trends in the United States, 1932–97, *J. Clim.*, 13(20), 3625–3637.

Sampe, T., and S. P. Xie (2010), Large-Scale dynamics of the Meiyu-baiu rainband: environmental forcing by the Westerly Jet, *J. Clim.*, 23 (1), 113–134.

Shen, Y., and A. Y. Xiong (2015), Validation and comparison of a new gauge-based precipitation analysis over mainland China, *Int. J. Climatol.*,36(1), 252–265, doi:10.1002/joc.4341.

Schreck, C. J., H. T. Lee, and K. Knapp (2018), HIRS outgoing longwave radiation—daily climate data record: Application toward identifying tropical subseasonal variability, *Remote Sens*., 10, 1325, doi:10.3390/rs10091325.

Timmermans, T., M. Wehner, and D. Cooley (2019), An evaluation of the consistency of extremes in gridded precipitation data sets, *Clim. Dyn.*, 52(11),52(11), 6651–6670, doi:10.1007/s00382-018-4537-0.

Takaya, K., and H. Nakamura (2001), A Formulation of a phase-independent wave-activity flux for stationary and migratory quasigeostrophic eddies on a zonally varying basic flow, *J. Atmos. Sci.*, 58, 608-627.

Touma, D., A. M. Michalak, D. L. Swain, and N. S. Diffenbaugh (2018), Characterizing the spatial scales of extreme daily precipitation in the United States, *J. Clim.*, 31(19), 8023–8037, doi:10.1175/JCLI-D-18-0019.1.

Toussaint, G. (1983), Solving geometric problems with the rotating calipers. *In Proceedings of the IEEE*, Athens, Greece.

Wang, J. Q., and M. S. Hu (1993), Distribution of extreme values of areal rainstorms in China, *Adv. Wat. Sci.*, 4(1), 1–9. (in Chinese)

Wang, Y. Q. (2012), wContour: A .NET class library of contour-related algorithms, *Comput. Geosci.*, 48, 330–333.

White, R. H., D. S. Battisti, and G. Skok (2017), Tracking precipitation events in time and space in gridded observational data, *Geophys. Res. Lett.*, 44, 8637–8646.

Xie, Z. Q., Y. Du, Y. Zeng, and Q. Miao (2018), Classification of yearly extreme precipitation events and associated flood risk in the Yangtze-Huaihe River Valley, *Sci. China. Earth. Sci.*, 61: 1341–1356, doi:10.1007/s11430-017-9212-8.

Yang, M. G., X. Chen, and S. Q. Cheng (2016), Hydrological impacts of precipitation extremes in the Huaihe River Basin, China, *SpringerPlus*, 5, 1731.

Zhou, B., P. Liang, D. Q. Wang, Y. H. Zhou, M. Xu, Y. Xiang, and M. R. Qin (2017), Meiyu monitoring indices (in Chinese), *National Standard of the People's of China*, GB/T33671–2017.

Zhou T. J., D. Y. Gong, J. Li J, and B. Li (2009), Detecting and understanding the multi-decadal variability of the East Asian Summer Monsoon recent progress and state of affairs. *Meteorol Z*, 18:455–467.

Table 1. Statistical characteristics of spatial scales of different types of HMPE

Period	Rain-belts	Orientation	Orientation range (°)	Averaged orientation (°)	Sample size	Extent (104km2)	Length (km)	Width (km)
1955–2015	50mm	Zonal pattern	0.0–13.2	5.4	255	37.2	1308.6	513.3
		Tilted pattern	13.2–35.0	20.9	196	41.2	1437.5	562.5
		Meridional pattern	35.0–90.0	49.6	38	40.8	1315.7	618.9
		All patterns	0.0–90.0	14.8	489	40	1373	541.1
1955–2015	100mm	Zonal pattern	0.0–13.2	4.8	198	12.9	788.8	278.7
		Tilted pattern	13.2–35.0	21.5	97	14.5	900.6	297.8
		Meridional pattern	35.0–90.0	48.1	16	12.6	784	291.2
		All patterns	0.0–90.0	13.4	310	13.4	823.5	285.3

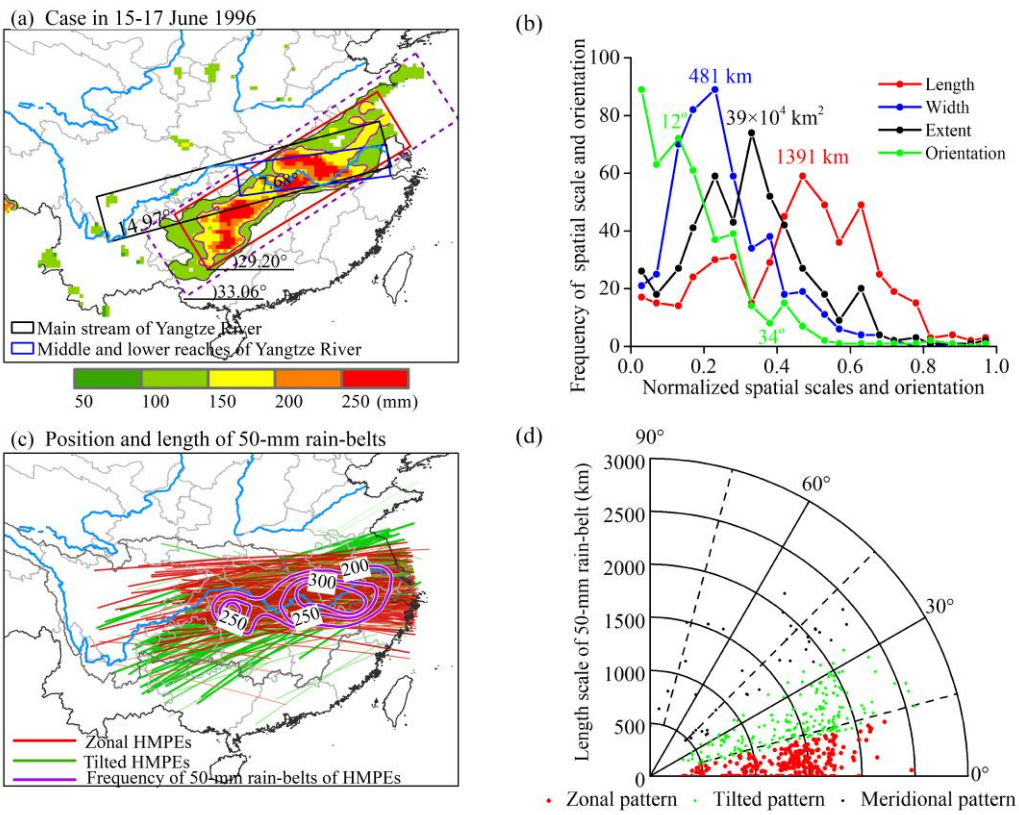

Figure 1. Example case (a), sample distributions of the spatial scale and orientation (b), frequencies and positions of 50-mm rain-belts (c), and lengths and orientations of different HMPE types (d).

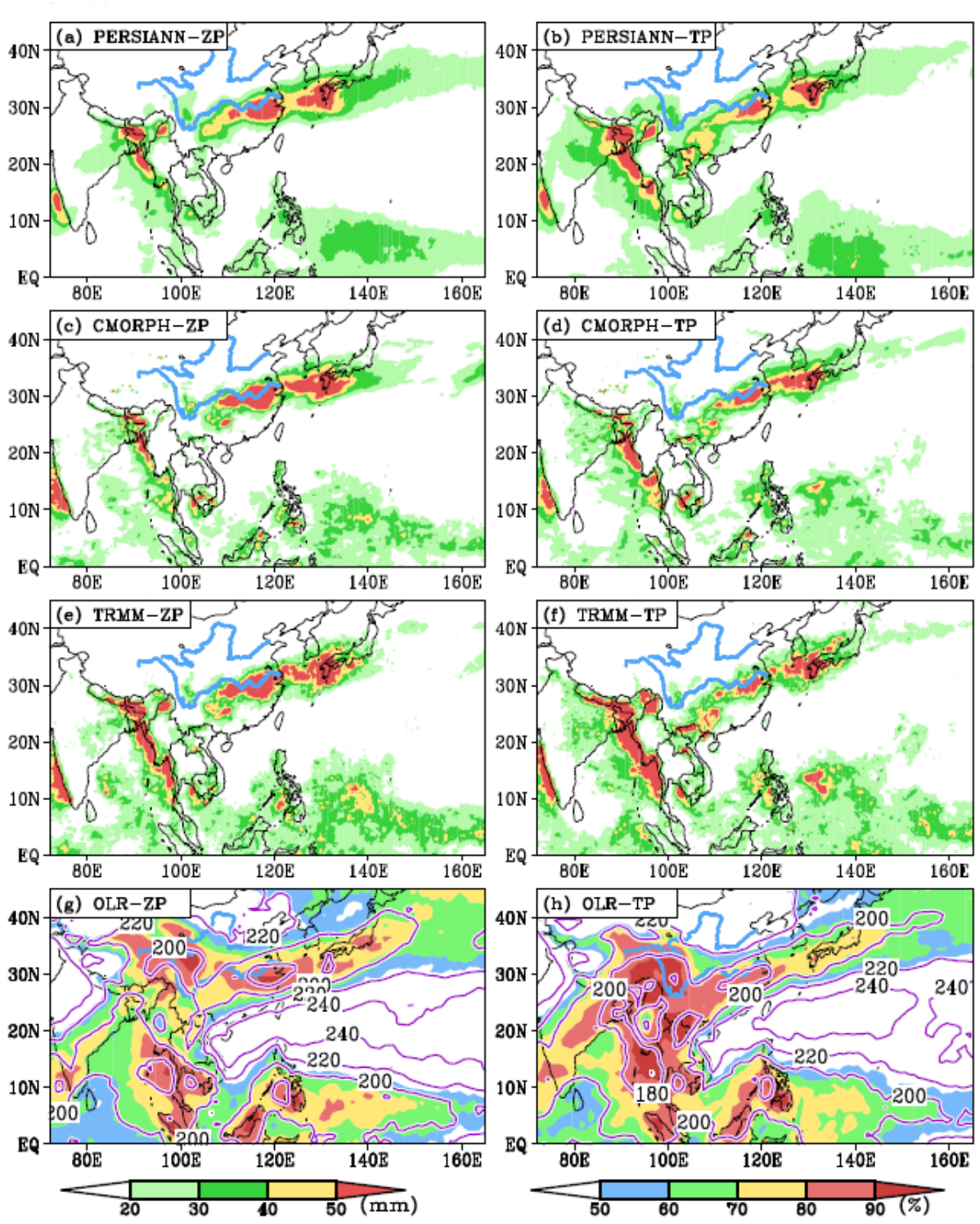

Figure 2. Average precipitation in PERSIANN for 1983–2015 (a–b) and CMORPH and TRMM for 1998–2015 (c–f), average (contour) and proportion of values below 240 W m^{-2} (shading) of outgoing longwave radiation (g–h) for zonal (left panel) and tilted (right panel) HMPEs.

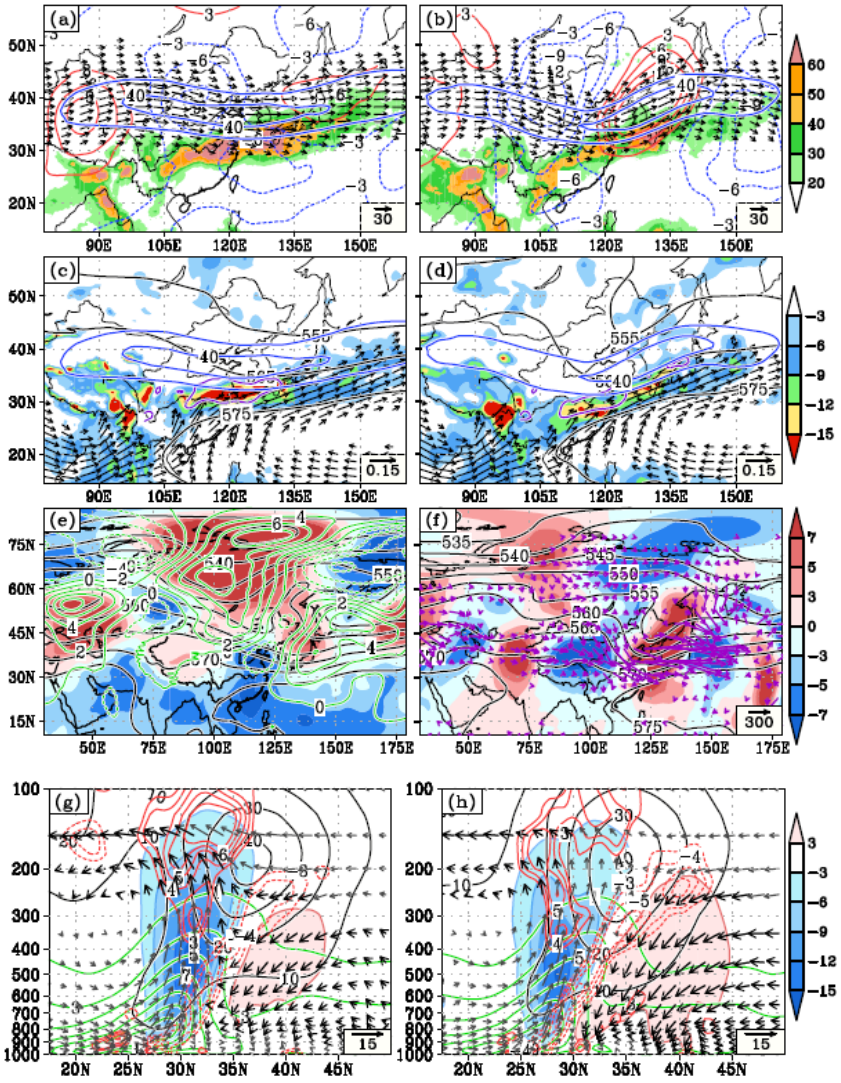

Figure 3. Distributions of rainfall (shading, mm) and 200-hPa wind fields (vector, m s^{-1}) and their zonal and meridional components (thick and thin contours) (a–b); 500-hPa heights (black contour, dagpm) (c–f); 500-hPa vertical velocities (shading, 10^{-2} Pa s^{-1}), 850-hPa vapor fluxes (vector, g $kg^{-1}s^{-1}$), equivalent potential temperature meridional gradient $\left|\frac{\partial \theta_e}{\partial y}\right|$exceeding 3 °C per 100 km (purple contour), and 200-hPa jet stream (blue contour, m s^{-1}) (c–d); anomalies of the 500-hPa height (green contour, dagpm) and total atmospheric sensible heating (shading, 10^6 W m^{-2}) (e); meridional wind anomalies (shading, m s^{-1}) and Rossby wave activity flux (vector, m^2 s^{-2}) at the 200-hPa level (f); latitude–height cross sections for 110°E–123°E (g–h) of vertical velocity (shading, 10^{-2} Pa s^{-1}), vapor fluxes (green contour, gm $kg^{-1}s^{-1}$), divergence (red contour, 10^{-6} s^{-1}), and zonal (black contour) and meridional winds (arrows represent winds and color represents the sign of $\mathbf{V}\cdot\nabla T$, the gray/black vectors denote warm/cold air intrusion, m s^{-1}). All left/right panels show zonal/tilted HMPEs for the period 1983–2015.